begindocument/before

Quantum metric nonlinear Hall effect in a topological antiferromagnetic heterostructure

Anyuan Gao,[1] Yu-Fei Liu,[1,2] Jian-Xiang Qiu,[1] Barun Ghosh,[3] Thaís V. Trevisan,[4,5] Yugo Onishi,[6] Chaowei Hu,[7] Tiema Qian,[7] Hung-Ju Tien,[8] Shao-Wen Chen,[2] Mengqi Huang,[9] Damien Bérubé,[1] Houchen Li,[1] Christian Tzschaschel,[1] Thao Dinh,[1,2] Zhe Sun,[1,10] Sheng-Chin Ho,[1] Shang-Wei Lien,[8] Bahadur Singh,[11] Kenji Watanabe,[12] Takashi Taniguchi,[12] David C. Bell,[13,14] Hsin Lin,[15] Tay-Rong Chang,[8] Chunhui Rita Du,[9] Arun Bansil,[3] Liang Fu,[6] Ni Ni,[7] Peter P. Orth,[4,5] Qiong Ma,[10] and Su-Yang Xu*[1]

[1]*Department of Chemistry and Chemical Biology, Harvard University, Massachusetts 02138, USA*

[2]*Department of Physics, Harvard University, Cambridge, MA 02138, USA*

[3]*Department of Physics, Northeastern University, Boston, MA 02115, USA*

[4]*Department of Physics and Astronomy, Iowa State University, Ames, Iowa 50011, USA*

[5]*Ames National Laboratory, Ames, Iowa 50011, USA*

[6]*Department of Physics, Massachusetts Institute of Technology, Cambridge, MA 02139, USA*

[7]*Department of Physics and Astronomy and California NanoSystems Institute, University of California, Los Angeles, Los Angeles, CA 90095, USA.*

[8]*Department of Physics, National Cheng Kung University, Tainan 701, Taiwan*

[9]*Department of Physics, University of California, San Diego, La Jolla, CA, 92093, USA*

[10]*Department of Physics, Boston College, Chestnut Hill, MA, USA*

[11]*Department of Condensed Matter Physics and Materials Science, Tata Institute of Fundamental Research, Colaba, Mumbai, India*

[12]*International Center for Materials Nanoarchitectonics, National Institute for Materials Science, 1-1 Namiki, Tsukuba 305-0044, Japan*

[13]*Harvard John A. Paulson School of Engineering and Applied Sciences, Harvard University, Cambridge, Massachusetts 02138, USA*

[14]*Center for Nanoscale Systems, Harvard University, Cambridge, Massachusetts 02138, USA*

* Corresponding author (email): suyangxu@fas.harvard.edu

[15]*Institute of Physics, Academia Sinica, Taipei 11529, Taiwan*

Quantum geometry is central to modern condensed matter physics. Due to the quantum nature, quantum geometry has two parts, the real part quantum metric and the imaginary part Berry curvature. Berry curvature has led to countless breakthroughs, ranging from the quantum Hall effect in 2DEGs to the anomalous Hall effect (AHE) in ferromagnets. In contrast, the quantum metric has rarely been explored. Here, we report a new nonlinear Hall effect induced by quantum metric dipole by interfacing even-layered $MnBi_2Te_4$ with black phosphorus. Like the AHE brought Berry curvature under the spotlight, our results open the door to discovering quantum metric responses. Moreover, our data suggests that the AFM can harvest wireless electromagnetic energy, potentially enabling applications that bridges nonlinear electronics with AFM spintronics.

Introduction

Nonlinearities are crucial in many branches of physics, ranging from atomic physics to condensed matter and complex dynamical systems. Nonlinear electrical transport is the foundation of applications such as rectification and wave mixing. Classically, the most well-known nonlinear device is a PN diode (Fig. 1A). Noncentrosymmetric polar materials (Fig. 1B) are similar to PN diodes as they both possess an electric dipole. They have recently been discovered to show intrinsic nonlinear electrical transport, which not only suggests novel nonlinear applications but also provides a powerful probe of the quantum geometry of the conduction electrons [1–16]. Broadly, the nonlinear transport in both diodes (Fig. 1A) and noncentrosymmetric conductors (Fig. 1B) arise from an inversion asymmetric charge distributions (e.g. an electric dipole). Since the electron has another fundamental degree of freedom, spin, an interesting question is whether spin can also lead to an electrical nonlinearity even in a centrosymmetric lattice. One ideal platform is the $\mathcal{PT}$-symmetric AFMs [17], where only the spins feature a noncentrosymmetric distribution (Fig. 1C).

Important clues can be drawn from previous optical experiments, where optical second-harmonic generation (SHG) has been observed in the $\mathcal{PT}$-symmetric AFMs including Cr_2O_3 and CrI_3 [18]. Nevertheless, nonlinear transport is distinct because it directly probes the Fermi surface electrons and in many cases their geometrical properties [1, 2]. As such, it enables a probe of the quantum geometry [1, 2] of the topological bands at the Fermi level of novel conductors.

The quantum geometry has two parts, $T = g + i\Omega$ [1] (T is the quantum geometrical tensor). The imaginary part is the well-known Berry curvature $\Omega_{\alpha\beta} = -2\mathrm{Im}\sum_{m\neq n}[\langle u_n|i\partial_{k_\alpha}u_m\rangle\langle u_m|i\partial_{k_\beta}u_n\rangle]$, which describes the curvature of wavefunction in Hilbert space (n, m are band indices and

α, β are spatial directions). Berry curvature has been identified as the source of many novel electronic and optical responses. By contrast, the real part is the quantum metric, $g_{\alpha\beta} = \mathrm{Re}\sum_{m\neq n}[\langle u_n|i\partial_{k_\alpha}u_m\rangle\langle u_m|i\partial_{k_\beta}u_n\rangle]$, which measures the distance between neighboring Bloch wavefunctions in Hilbert space (i.e., the distance when Bloch wavefunctions are mapped onto a Bloch sphere, see [19]. IV.2). Although being equally important, the quantum metric is much less explored. There have been a few examples related to the quantum metric, including prediction for the electrical and orbital magnetic susceptibilities [20], observation of a third order Hall effect [13] and the quantum metric in atomic physics [21]. However, examples have remained limited and how quantum metric regulates the electronic motion remains largely unknown. Recently, theory has started to predict a wide range of exotic quantum metric responses [20, 22–34].

Here, we report the observation of the quantum metric dipole induced second-order anomalous Hall effect (AHE) [20, 22–25]. In the past decades, there have been numerous studies of the AHE (both linear and nonlinear) induced by Berry curvature. Recent theoretical studies, however, predict that quantum metric can also lead to AHE, therefore advancing our understanding of the fundamental origin of the AHE. Distinct from the Berry curvature induced AHEs, this new effect is predicted to exist in the $\mathcal{PT}$-symmetric AFMs [20, 22–25], where $\mathcal{PT}$ forces the Berry curvature to vanish identically but the effects of quantum metric can manifest strongly. We design and fabricate a feasible material platform and demonstrate the first realization of this quantum metric nonlinear Hall effect. We show that it exhibits distinctly different properties compared to the nonlinear Hall effect induced by Berry curvature dipole in noncentrosymmetric crystals. To conceptualize this new nonlinear Hall effect, we draw comparison with the well-known AHE in ferromagnetic metals [35], where Berry curvature leads to the anomalous velocity and therefore the AHE, $v_{\text{anomalous}} \propto \int_{\mathbf{k}} \mathbf{E}_\parallel \times \mathbf{\Omega}$, ($\mathbf{E}_\parallel$ is the in-plane source-drain electric field). By contrast, in a $\mathcal{PT}$-symmetric AFM, Berry curvature is zero due to $\mathcal{PT}$. However, a nonzero quantum metric g can induce an anomalous velocity to the second-order of $\mathbf{E}_\parallel$, $v_{\text{anomalous}} \propto \int_{\mathbf{k}} \mathbf{E}_\parallel \times [\nabla_k \times (\mathbf{g}\mathbf{E}_\parallel)]$, as proposed in [20]. This leads to the intrinsic second-order Hall effect. From the expression above, one can show that this effect is nonzero only when the system breaks both $\mathcal{P}$ and $\mathcal{T}$. Therefore, we need $\mathcal{PT}$-symmetric AFM conductors with a large quantum metric on the Fermi surface. We have carefully considered possible materials, and identified 2D even-layered $MnBi_2Te_4$ [15, 36–38, 38–46] as an ideal platform. Even-layered $MnBi_2Te_4$ is a $\mathcal{PT}$-symmetric AFM. Moreover, its topological bands support gate-tunable transport and a giant quantum metric. However, its lattice has $\mathcal{C}_{3z}$ rotational symmetry (Figs. 1D,E), which forces the effect to vanish [22]. To break C_{3z}, we interface it with black phosphorus (BP) [47].

Demonstration of rotational symmetry breaking

We start by showing that interfacing $MnBi_2Te_4$ with BP indeed breaks its $\mathcal{C}_{3z}$ rotational symmetry. To this end, we study the directional dependence of the resistance [6] of $MnBi_2Te_4$ without and with BP. We fabricated a 6-septuple-layer (6SL) $MnBi_2Te_4$ device with radially distributed electrical contacts (Device-BM1). As shown by the blue curve in Fig. 1G, the four-probe resistance ($T = 1.8$ K) is found to be fully isotropic, consistent with the presence of the $\mathcal{C}_{3z}$ symmetry. We then stacked a BP layer (~ 10 nm) onto this $MnBi_2Te_4$ sample and performed the measurements again. As shown by the red curve in Fig. 1G, the resistance develops a clear anisotropy with a 180° periodicity, providing a clear signature of the breaking of $\mathcal{C}_{3z}$ symmetry (In [19]. I.3, we present additional experiments to show that the transport signal is dominated by the $MnBi_2Te_4$ layer of the heterostructure). The transverse resistance and two-probe resistance also show the breaking of $\mathcal{C}_{3z}$ (fig. S12). We further substantiate the breaking of $\mathcal{C}_{3z}$ symmetry by an independent method, the optical second harmonic generation (SHG) at room temperature. As shown in Fig. 1H, our SHG data also shows the clear breaking of $\mathcal{C}_{3z}$ symmetry (see detailed discussions in SM. I.5 and fig. S13). Our demonstration of $\mathcal{C}_{3z}$ breaking establishes the BP/$MnBi_2Te_4$ heterostructure as an ideal platform to search for this effect.

Observation of the nonlinear Hall effect

In order to measure the linear and nonlinear electrical transport, we pass a current at frequency ω (I^{ω}) and use the lock-in technique to detect linear voltage V^{ω} and nonlinear voltage $V^{2\omega}$. We describe the nonlinear voltage as $V^{2\omega}_{ijk}$, where i is the direction of the nonlinear voltage $V^{2\omega}$ and j, k are the directions of the injected current I^{ω}. All measurements are performed at $B = 0$.

Figure 1I shows the nonlinear Hall voltage $V^{2\omega}_{yxx}$ of the Device-BM1 before and after interfaced with BP. Remarkably, a prominent nonlinear Hall signal only emerges after BP is introduced. This is in sharp contrast to the linear voltage (inset of Fig. 1I), which becomes even slightly smaller upon the introduction of BP. Such observation agrees well with the theoretical expectation of the intrinsic nonlinear Hall effect induced by a quantum metric dipole. To exclude that the effect is caused by a Berry curvature dipole [4, 6, 7, 9], which leads to a second-order Hall effect in nonmagnetic, noncentrosymmetric conductors, we study the relationship between the second-order nonlinear Hall effect and the AFM order in $MnBi_2Te_4$.

The AFM spin-induced nonlinearity

Overall, we have fabricated 30 BP/even-layered $MnBi_2Te_4$ heterostructure devices (see SM.I.0

for our systematic data that confirm the $MnBi_2Te_4$ thickness in our devices). In all of the 30 devices, we have observed the nonlinear Hall effect with consistent behaviors as a function of AFM order, spatial direction, scattering time, vertical electric field and doping (see fig. S22 and table S1 for a summary of all 30 devices). Here, we focus on the Device-BMB1 (Fig. 2A), which has 2L BP on both sides of 6SL $MnBi_2Te_4$. Moreover, we have made sure that the crystalline a axes of the BPs and the $MnBi_2Te_4$ are all aligned (Fig. 2A). Such a carefully controlled configuration is important to preserve $MnBi_2Te_4$'s $\mathcal{PT}$ symmetry, which enforces the Berry curvature and Berry curvature dipole to vanish. Figure 2B shows the basic nonlinear transport responses. A large transverse nonlinear response $V_{yxx}^{2\omega}$ is found, showing the nonlinear Hall effect in Device-BMB1. We have also measured the longitudinal nonlinear response $V_{xxx}^{2\omega}$, which shows no observable signal. Therefore, our data reveals an interesting "Hall dominance" in the nonlinear transport.

We now focus on exploring how the nonlinear Hall signal depends on opposite AFM states. In ferromagnets, the opposite FM states can be controlled by sweeping B field. In $\mathcal{PT}$-symmetric AFMs including Cr_2O_3, even-layered CrI_3 and even-layered $MnBi_2Te_4$ [44, 48, 49], previous works have shown that the opposite AFM states can be controlled by sweeping vertical B_z field under a fixed vertical E_z field. Hence, we follow the procedures established by previous works [44]: under a fixed E_z ($E_z = -0.17$ V/nm), we sweep B_z from -8 T to 0 T or from $+8$ T to 0 T to prepare the two AFM states (Fig. 2, C and D). We first study the AFM-I. The linear voltage V_{xx}^{ω} (Fig. 2E) exhibits a typical Ohm's law behavior. The nonlinear voltage $V_{yxx}^{2\omega}$ (Fig. 2G) is prominent and its sign is positive. We then prepare AFM-II. The linear voltage V_{xx}^{ω} (Fig. 2F) remains unchanged. In sharp contrast, the nonlinear voltage $V_{yxx}^{2\omega}$ (Fig. 2H) flips sign. For both AFM-I and II, if we measure $V_{yxx}^{2\omega}$ while warming up, we found that the nonlinear Hall effect is only present in the AFM phase but is absent in the nonmagnetic phase (Fig. 2, I and J). Our observation that the nonlinear Hall signal flips sign upon reversing the AFM order further demonstrates its quantum metric dipole origin, because the quantum metric dipole is theoretically expected to be opposite for the opposite AFM domains (see SM.III). In addition, we note that our nonlinear Hall signal measures an average over all AFM domains. On the other hand, our experiments suggest that our sample is prepared into predominantly one domain. If our sample consists of opposite domains with 50%-50% composition, then the measured nonlinear Hall signal would average to zero. In contrast, our data show large nonzero nonlinear Hall signal. Moreover, the sign of the observed signal flips as we prepare the opposite AFM domain. Further, the magnitude of the measured signal is consistent with the theoretically calculated value, which assumes a single domain. These facts combined suggest that our sample is prepared into one predominant domain. Future spatially-

resolved magnetic measurements will be interesting to determine the exact domain composition.

We now perform further systematic studies. Because the nonlinear Hall current flips sign upon reversing the AFM order, all the nonlinear Hall data (apart from Fig. 2) are obtained by taking the difference between the two AFM domains. First, the intrinsic nonlinear Hall effect is expected to be independent of the scattering time. Interestingly, this represents the first known nonlinear transport effect that is independent of scattering. Note that similar to the intrinsic AHE in ferromagnetic metals [35], there is still dissipation through the linear Drude conductivity σ_{xx}. So they are different from the QAHE that has no dissipation channel at all. The nonlinear Hall conductivity can be directly extracted from our data by $\sigma^{2\omega}_{yxx} = J^{2\omega}_{yxx}/E^{\omega 2}_{x} = \frac{V^{2\omega}_{yxx}}{I^{\omega 2}_{x} R^{3}_{xx}} \frac{l^3}{w^2 d}$, where l, w, d are the length, width and thickness of the sample. Previous experiments have studied the scattering time τ dependence of various Hall effects [6, 9, 14, 35] by investigating the scaling between the corresponding Hall conductivity and the Drude conductivity. Therefore, following the established method, we study the scaling between $\sigma^{2\omega}_{yxx}$ and σ_{xx}. Our data (Fig. 3A) show that $\sigma^{2\omega}_{yxx}$ is independent of σ_{xx} below $\sim$ 15 K. Moreover, consistent results have been observed at multiple charge densities in the same sample and from different samples (SM.III.9). These systematic data point to the conclusion that the $\sigma^{2\omega}_{yxx}$ is independent of scattering time τ below $\sim$ 15 K. Above $\sim$ 15 K, $\sigma^{2\omega}_{yxx}$ vanishes quickly across T_{N} because the AFM order vanishes and our nonlinear Hall effect only exists in the AFM phase. Hence studying the τ dependence at temperatures near T_{N} would require one to take the strong influence of the AFM order near T_{N} into account (see SM.III.8 for additional measurements and analysis). Second, the intrinsic nonlinear Hall effect does not require a noncentrosymmetric lattice or any explicit breaking of $\mathcal{PT}$ symmetry. To test this, we explicitly break $\mathcal{PT}$ by applying a vertical E_z field via dual gating. As shown in Fig. 3D, the nonlinear Hall signal is already prominent even at $E_z = 0$, confirming that it does not require any $\mathcal{PT}$ breaking. Moreover, the nonlinear Hall signal is symmetric for $\pm E_z$, also consistent with the expectation (see SM. IV.3). Third, the nonlinear Hall effect is expected to be sensitive to the direction of the incident current I^{ω}. In Fig. 3B, we measure the nonlinear Hall conductivity as a function of the direction of I^{ω}. Indeed, we found that the signal is most prominent when I^{ω} is along a particular in-plane direction. In this way, we managed to experimentally map out the direction of the relevant geometrical dipole (in our case it is the quantum metric dipole as we demonstrate next). Moreover, the intrinsic nonlinear Hall effect is expected to be independent of frequency. In SM.III.2, we present additional experiment which confirms that our nonlinear Hall signal is indeed frequency independent for the tested range. In principle, due to its independence of τ, the intrinsic nonlinear Hall effect is expected

to persist all the way until $\hbar\omega$ is large enough to induce an inter-band transition (roughly terahertz or far-infrared). Future experiments are needed to test the nonlinear Hall effect in that regime.

Demonstrating the quantum metric mechanism by excluding competing mechanisms

Although we tried to eliminate Berry curvature dipole by aligning the crystalline a axes between BPs and $MnBi_2Te_4$ to preserve $\mathcal{PT}$ symmetry (Fig. 2A), let us assume that the alignment is imperfect, so Berry curvature dipole is allowed. We now show that the observed relationship between the nonlinear Hall signal and AFM order can discern Berry curvature dipole D_{Berry} and quantum metric dipole D_{Metric} [22]. D_{Berry} can be understood as a distribution of the Berry curvature around the Fermi surface such that it is larger on one side of the Fermi surface than on the opposite side. A similar picture holds for D_{Metric} (Fig. 3). As we observe that the nonlinear Hall signal changes sign upon the reversal of AFM order, the dipole that causes our observed nonlinear Hall signal must also flip. Let us assume that the AFM-I has $D_{\text{Berry}} > 0$ and $D_{\text{Metric}} > 0$, which is visualized in a tilted gapped Dirac band structure in Figs. 3E and G. We now flip the AFM order to the AFM-II by performing time reversal $\mathcal{T}$. Under $\mathcal{T}$, the bands are flipped between $\pm\mathbf{k}$ (Figs. 3F-H), the Berry curvature flips sign ($\Omega(k) \xrightarrow{\mathcal{T}} -\Omega(-k)$), but the quantum metric keeps the same sign ($g(k) \xrightarrow{\mathcal{T}} g(-k)$). Hence, from Figs. 3F-H, one can see that, $D_{\text{Berry}}(\text{AFM-II}) = D_{\text{Berry}}(\text{AFM-I})$, but $D_{\text{Metric}}(\text{AFM-II}) = -D_{\text{Metric}}(\text{AFM-I})$. Therefore, our observation that the nonlinear Hall signal flips sign upon reversing the AFM order excludes the Berry curvature dipole mechanism. In SM.II.1, we present thorough analysis to enumerate systematic experimental results including the relation with AFM order, scaling, vertical electric field dependence and relation with mirror symmetry, which further corroborate that the Berry curvature dipole mechanism cannot account for our data.

Within the nonlinear effects that flip sign upon reversing the AFM order, there is another possibility, the second-order Drude effect [5, 12, 17, 22]. This effect can be ruled out based on our scaling data in Fig. 3A, because it is expected to be proportional to τ^2 [22]. Moreover, the nonlinear Hall effect (NHE) is antisymmetric (upon exchanging the first two indices) $\sigma^{\text{NHE}}_{\alpha\beta\gamma} = -\sigma^{\text{NHE}}_{\beta\alpha\gamma}$ but the second-order Drude effect (SODE) is symmetric $\sigma^{\text{SODE}}_{\alpha\beta\gamma} = \sigma^{\text{SODE}}_{\beta\alpha\gamma}$ [22]. Using a novel electrical sum-frequency generation method (SM. II.2), we showed that our signal is indeed antisymmetric, i.e., $\sigma^{2\omega}_{yxx} = -\sigma^{2\omega}_{xyx}$, which demonstrates that the SODE is insignificant in our signal (SM II.2). In SM.II.2.3, we present additional data which suggests that the NHE is dominant over the SODE at different temperatures and charge densities. In SM.III.5, we show that the nonlinear Hall signal is negligibly small at ± 8 T because the forced FM state recovers inversion symmetry. Finally, we also carefully addressed other competing origins such as thermal (including current-induced

overall temperature increase) and accidental diode junctions (SM. II.3). By excluding competing mechanisms, we establish the quantum metric dipole as the underlying interpretation.

Energy-resolved probe of quantum metric in $\mathcal{PT}$-symmetric AFM

We also study the evolution of the nonlinear conductivity $\sigma_{yxx}^{2\omega}$ with the charge density n. As shown in Fig. 4A, the nonlinear Hall signal is zero inside the charge neutrality gap. This is consistent with the expectation that the nonlinear Hall effect is a Fermi surface property. As we tune the Fermi energy away from the charge neutrality, the nonlinear Hall signal emerges. Importantly, the conductivity in electron and hole regimes have the same sign. As we go deeper into the electron-doped regime, the signal reverses sign.

We now provide an intuitive physical picture to understand the large quantum metric dipole and its Fermi level dependence. $MnBi_2Te_4$ features Dirac surface states, which are gapped due to the AFM, leading to large quantum metric near the gap edge. Moreover, because the AFM order breaks both $\mathcal{T}$ and $\mathcal{P}$, the Dirac bands are asymmetric about $\mathbf{k} = 0$, as shown in Fig. 3G. Hence, at a fixed energy, positive and negative momenta have different quantum metric, leading to a nonzero quantum metric dipole. Intuitively, we can understand the sign of the nonlinear Hall signal by which momentum side has a larger quantum metric. We see from Fig. 3G that both upper and lower parts of the Dirac cone have $g(+k_{\mathrm{F}}) > g(-k_{\mathrm{F}})$, suggesting that the nonlinear Hall signals should show the same sign in electron and hole regimes, consistent with our data (Fig. 4A). The sign change in the electron-doped regime is beyond this simple picture.

To achieve a more comprehensive understanding, we built an effective model of the BP/6SL $MnBi_2Te_4$/BP heterostructure (SM.IV.4-9). Due to the incommensurability of the BP and $MnBi_2Te_4$ lattices, we need to derive the coupling between the Bloch states of the two materials in the real-space continuum (i.e. within the extended Brillouin zone BZ). The low-energy bands are located in the BZ center Γ, so only Bloch bands with the same momentum hybridize. The coupling amplitude depends only on the characteristic decay length of the atomic orbitals as any discrete lattice structure is averaged out [47]. The Hamiltonian reads $\hat{h}(k_x, k_y) = \begin{pmatrix} \hat{h}_{\mathrm{MBT}} & \hat{U}_t & \hat{U}_b \\ \hat{U}_t^\dagger & \hat{h}_{\mathrm{BP},t} & 0 \\ \hat{U}_b^\dagger & 0 & \hat{h}_{\mathrm{BP},b} \end{pmatrix}$. $\hat{h}_{\mathrm{MBT}}$ and $\hat{h}_{\mathrm{BP},t(b)}$ are Hamiltonians for 6SL $MnBi_2Te_4$ and top (bottom) BP. The spin-orbit coupling (SOC) in $MnBi_2Te_4$ is crucial for a nonzero nonlinear Hall effect because it allows the low-energy orbitals to feel the symmetry breaking by the AFM order (SM.III.15). In particular, the SOC was included in the model following the original work by Ref. [50] . $\hat{U}_t$ and $\hat{U}_b$ denote the band hybridization due to nearest-neighbors coupling between $MnBi_2Te_4$ and BP. The bare $MnBi_2Te_4$ and BP parameters were obtained by fitting the first-principle band structures. The $MnBi_2Te_4$ and

BP coupling parameters were partly constrained by considering the independent data of R_{xx}/R_{yy} so that an agreement in the overall magnitude was achieved independently. There are still free coupling parameters in the model which we adjusted to match detailed features in the charge density dependence (SM.IV.9) .

We first turn off the coupling between the $MnBi_2Te_4$ and BP ($\hat{U}_t = \hat{U}_b = 0$). The Fermi surface shown in Fig. 4C (-50 meV) is C_{3z} symmetric and there are already large quantum metric (g_{xx} and g_{yx}) around it. According to Ref. [22], the D_{Metric} responsible for the nonlinear Hall is given by $D_{\text{Metric}} = \int_{\mathbf{k}}(v_y g_{xx} - v_x g_{yx})\delta(\varepsilon - \varepsilon_{\text{F}})$ (v is the Fermi velocity).We plot the integral kernel $(v_y g_{xx} - v_x g_{yx})$ as color in Fig. 4D. Positive and negative contributions around the contour exactly cancel because of C_{3z} symmetry. So the integral goes to zero (the left panel in Fig. 4D). We then turn on the $MnBi_2Te_4$-BP couplings, which breaks C_{3z}. For the C_{3z}-breaking contour, we observe unequal contributions from the two colors, leading to a nonzero D_{Metric} (the right panel in Fig. 4D, see details in the caption and in SM.III.14). Figure 4E shows the band structure of the BP/6SL $MnBi_2Te_4$/BP heterostructure, based on which we can compute the intrinsic nonlinear Hall conductivity $\sigma^{2\omega}_{yxx}$ as a function of chemical potential. In particular, near the charge neutrality gap, we found that $\sigma^{2\omega}_{yxx}$ indeed mainly comes from the quantum metric of the Dirac surface states, consistent with the intuitive picture above. The sign inversion in the electron-doped regime mainly comes from the quantum metric of the avoided crossing inside conduction bands according to our calculation (SM.IV.9) . Note that due to the multiband nature of our model, the $\sigma^{2\omega}_{yxx}$ was calculated by the general expression $\sigma^{2\omega}_{yxx} = 2e^3 \sum_{n,m}^{\varepsilon_n \neq \varepsilon_m} \text{Re} \int_{\mathbf{k}} \big(\frac{v_y^n \langle u_n | i\partial_{k_x} u_m \rangle \langle u_m | i\partial_{k_x} u_n \rangle}{\varepsilon_n - \varepsilon_m} - \frac{v_x^n \langle u_n | i\partial_{k_y} u_m \rangle \langle u_m | i\partial_{k_x} u_n \rangle}{\varepsilon_n - \varepsilon_m} \big) \delta(\varepsilon_n - \varepsilon_{\text{F}})$ [22]. This general expression can be decomposed into the quantum metric dipole D_{Metric} contribution plus additional inter-band contributions (AIC),

$$\sigma^{2\omega}_{yxx} = 2e^3 \sum_n \int_{\mathbf{k}} \frac{v_y^n g_{xx}^n - v_x^n g_{yx}^n}{\varepsilon_n - \varepsilon_{\bar{n}}} \delta(\varepsilon_n - \varepsilon_{\text{F}}) + \text{AIC}, \tag{1}$$

where the first term is the quantum metric dipole contribution, and the second term is AIC $= 2e^3 \sum_{n,m}^{\varepsilon_m \neq \varepsilon_n, \varepsilon_{\bar{n}}} \text{Re} \int_{\mathbf{k}} \big(\frac{v_y^n \langle u_n | i\partial_{k_x} u_m \rangle \langle u_m | i\partial_{k_x} u_n \rangle}{\varepsilon_n - \varepsilon_m} - \frac{v_x^n \langle u_n | i\partial_{k_y} u_m \rangle \langle u_m | i\partial_{k_x} u_n \rangle}{\varepsilon_n - \varepsilon_m} \big) \frac{\varepsilon_m - \varepsilon_{\bar{n}}}{\varepsilon_n - \varepsilon_m} \delta(\varepsilon_n - \varepsilon_{\text{F}})$ ($\bar{n}$ is the band whose energy is closest to n). In our BP/6SL $MnBi_2Te_4$/BP system, we found that the quantum metric dipole contribution strongly dominates, whereas the AIC is small (see details in SM. IV.3). Therefore, our nonlinear Hall measurement is a powerful, energy-resolved probe of the quantum metric.

Possible AFM spin-based wireless rectification and outlook

The second-order nonlinear effect enables not only frequency doubling ($\omega \to 2\omega$) but also rectifi-

cation ($\omega \to$ DC). The rectification is crucial for harvesting electromagnetic radiation energy [9, 12] because we can convert the electromagnetic radiation into DC electricity. We use the intrinsic AFM nonlinear Hall effect to demonstrate wireless rectification with zero external bias (battery-free) and without magnetic field. We inject microwave radiation and measure the DC signal. As shown in Fig. 4F, we observe clear rectification DC voltage in response to the microwave radiation, which shows a broad band response, including the WiFi frequencies (2.4 GHz and 5 GHz) and even higher frequencies (see fig. S35. Also see SM.V.2 for a thorough analysis of the efficiency of the wireless rectification as well as its potential advantages and disadvantages). In SM.III.12, we show that the rectification signal flips sign as we reverse the AFM state, which suggests that the observed rectification arises from the intrinsic quantum metric dipole origin. We note that, apart from the intrinsic quantum metric dipole, extrinsic sources such as the the Schottky diodes at the metal-$MnBi_2Te_4$ junction, unintentional diodes inside the $MnBi_2Te_4$, and the gap between the two gates can also lead to microwave rectification. In order unambiguously rule out these extrinsic sources, future systematic experiments will be interesting (discussion in SM.V.1).

In summary, we have presented the first experimental realization of the intrinsic second-order Hall effect. This effect realizes an electrical nonlinearity induced by the AFM spins and provides a rare example of a quantum metric response. Both aspects are of fundamental interest. Just like the AHE about a decade ago inspired the discoveries of a variety of Berry curvature responses, we hope that our work opens the door to experimentally search for quantum metric responses. As highlighted by recent theoretical studies, the influence of the quantum metric is expected to span many different areas, ranging from nonlinear responses in $\mathcal{PT}$-symmetric AFMs to flat band conductivity, superconductivity and charge orders in moiré systems, the fractional Chern insulator, and $\mathbf{k}$-space dual of gravity [20, 22–34]. Another interesting future direction is to explore the nonlinear responses in canted AFM materials (SM.V.3) [38, 46, 51], where nonzero Berry curvature higher order to M have recently been observed. In terms of materials, the vdW interface engineering has been widely applied to engineer band structure, such as the band alignment in semiconductors. We show that, beyond "band structure engineering", the vdW interfaces can be used to engineer the properties of the wavefunction i.e., "quantum geometry engineering" [47]. We demonstrate that, the topological Dirac surface state on the interface of a TI can be the source of a wide range of novel topological and geometrical phenomena beyond the Berry curvature upon proper engineering. In terms of spin-induced electrical nonlinearity, our observation enables the possibility to use AFM spins to harvest electromagnetic energy and to realize self-powered AFM spintronic devices, potentially at low power density and high frequencies. An exciting future breakthrough

would be to demonstrate room temperature wireless rectification based on the quantum metric nonlinear Hall effect in a room temperature $\mathcal{PT}$-symmetric AFM material.

[1] J. Provost, G. Vallee, Riemannian structure on manifolds of quantum states, *Commun. Math. Phys.* **76**, 289 (1980).

[2] Y. Tokura, N. Nagaosa, Nonreciprocal responses from non-centrosymmetric quantum materials, *Nature Commun.* **9**, 1 (2018).

[3] J. E. Moore, J. Orenstein, Confinement-induced Berry phase and helicity-dependent photocurrents, *Phys. Rev. Lett.* **105**, 026805 (2010).

[4] I. Sodemann, L. Fu, Quantum nonlinear Hall effect induced by Berry curvature dipole in time-reversal invariant materials, *Phys. Rev. Lett.* **115**, 216806 (2015).

[5] T. Ideue, *et al.*, Bulk rectification effect in a polar semiconductor, *Nature Phys.* **13**, 578 (2017).

[6] K. Kang, T. Li, E. Sohn, J. Shan, K. F. Mak, Nonlinear anomalous Hall effect in few-layer WTe_2, *Nature Mater.* **18**, 324 (2019).

[7] Q. Ma, *et al.*, Observation of the nonlinear Hall effect under time-reversal-symmetric conditions, *Nature* **565**, 337 (2019).

[8] S. Dzsaber, *et al.*, Giant spontaneous Hall effect in a nonmagnetic Weyl-Kondo semimetal, *PNAS* **118**, e2013386118 (2021).

[9] D. Kumar, *et al.*, Room-temperature nonlinear Hall effect and wireless radiofrequency rectification in Weyl semimetal $TaIrTe_4$, *Nature Nanotech.* **16**, 421 (2021).

[10] K. Yasuda, *et al.*, Large non-reciprocal charge transport mediated by quantum anomalous Hall edge states, *Nature Nanotech.* **15**, 831 (2020).

[11] W. Zhao, *et al.*, Magnetic proximity and nonreciprocal current switching in a monolayer WTe_2 helical edge, *Nature Mater.* **19**, 503 (2020).

[12] H. Isobe, S.-Y. Xu, L. Fu, High-frequency rectification via chiral Bloch electrons, *Science Advances* **6**, eaay2497 (2020).

[13] S. Lai, *et al.*, Third-order nonlinear Hall effect induced by the Berry-connection polarizability tensor, *Nature Nanotech.* **16**, 869 (2021).

[14] P. He, *et al.*, Graphene moiré superlattices with giant quantum nonlinearity of chiral Bloch electrons, *Nature Nanotech.* **17**, 378 (2022).

[15] Z. Zhang, *et al.*, Non-reciprocal charge transport in an intrinsic magnetic topological insulator $MnBi_2Te_4$, *Nature Commun.* **13**, 6191 (2022).

[16] S. Sinha, *et al.*, Berry curvature dipole senses topological transition in a moiré superlattice, *Nature Phys.* 1–6 (2022).

[17] N. J. Zhang, *et al.*, Diodic transport response and the loop current state in twisted trilayer graphene Preprint at https://arxiv.org/abs/2209.12964 (2022).

[18] Z. Sun, *et al.*, Giant nonreciprocal second-harmonic generation from antiferromagnetic bilayer CrI_3, *Nature* **572**, 497 (2019).

[19] See additional text and data in supplementary materials.

[20] Y. Gao, S. A. Yang, Q. Niu, Field induced positional shift of Bloch electrons and its dynamical implications, *Phys. Rev. Lett.* **112**, 166601 (2014).

[21] A. Gianfrate, *et al.*, Measurement of the quantum geometric tensor and of the anomalous Hall drift, *Nature* **578**, 381 (2020).

[22] C. Wang, Y. Gao, D. Xiao, Intrinsic Nonlinear Hall Effect in Antiferromagnetic Tetragonal CuMnAs, *Phys. Rev. Lett.* **127**, 277201 (2021).

[23] H. Liu, *et al.*, Intrinsic Second-Order Anomalous Hall Effect and Its Application in Compensated Antiferromagnets, *Phys. Rev. Lett.* **127**, 277202 (2021).

[24] S. Lahiri, K. Das, D. Culcer, A. Agarwal, Intrinsic nonlinear conductivity induced by the quantum metric dipole Preprint at https://arxiv.org/abs/2207.02178 (2022).

[25] T. B. Smith, L. Pullasseri, A. Srivastava, Momentum-space gravity from the quantum geometry and entropy of Bloch electrons, *Phys. Rev. Research* **4**, 013217 (2022).

[26] A. Arora, M. S. Rudner, J. C. W. Song, Quantum metric dipole and non-reciprocal bulk plasmons in parity-violating magnets, *Nano Lett.* **22**, 9351 (2022).

[27] J. Mitscherling, T. Holder, Bound on resistivity in flat-band materials due to the quantum metric, *Phys. Rev. B* **105**, 085154 (2021).

[28] J.-W. Rhim, K. Kim, B.-J. Yang, Quantum distance and anomalous Landau levels of flat bands, *Nature* **584**, 59 (2020).

[29] P. J. Ledwith, G. Tarnopolsky, E. Khalaf, A. Vishwanath, Fractional Chern insulator states in twisted bilayer graphene: An analytical approach, *Phys. Rev. Research* **2**, 023237 (2020).

[30] T. Holder, D. Kaplan, B. Yan, Consequences of time-reversal-symmetry breaking in the light-matter interaction: Berry curvature, quantum metric, and diabatic motion, *Phys. Rev. Research* **2**, 033100 (2020).

[31] H. Watanabe, Y. Yanase, Chiral Photocurrent in Parity-Violating Magnet and Enhanced Response in Topological Antiferromagnet, *Phys. Rev. X* **11**, 011001 (2021).

[32] K.-E. Huhtinen, J. Herzog-Arbeitman, A. Chew, B. A. Bernevig, P. Törmä, Revisiting flat band superconductivity: Dependence on minimal quantum metric and band touchings, *Phys. Rev. B* **106**, 014518 (2022).

[33] J. S. Hofmann, E. Berg, D. Chowdhury, Superconductivity, charge density wave, and supersolidity in flat bands with tunable quantum metric Preprint at https://arxiv.org/abs/2204.02994 (2022).

[34] X. Hu, T. Hyart, D. I. Pikulin, E. Rossi, Quantum-metric-enabled exciton condensate in double twisted bilayer graphene, *Phys. Rev. B* **105**, L140506 (2022).

[35] N. Nagaosa, J. Sinova, S. Onoda, A. MacDonald, N. P. Ong, Anomalous Hall effect, *Rev. Mod. Phys.* **82**, 1539 (2010).

[36] M. M. Otrokov, *et al.*, Prediction and observation of an antiferromagnetic topological insulator, *Nature* **576**, 416 (2019).

[37] D. Zhang, *et al.*, Topological axion states in the magnetic insulator $MnBi_2Te_4$ with the quantized magnetoelectric effect, *Phys. Rev. Lett.* **122**, 206401 (2019).

[38] S. H. Lee, *et al.*, Spin scattering and noncollinear spin structure-induced intrinsic anomalous Hall effect in antiferromagnetic topological insulator $MnBi_2Te_4$, *Phys. Rev. Research* **1**, 012011 (2019).

[39] Y. Deng, *et al.*, Quantum anomalous Hall effect in intrinsic magnetic topological insulator $MnBi_2Te_4$, *Science* **367**, 895 (2020).

[40] C. Liu, *et al.*, Robust axion insulator and Chern insulator phases in a two-dimensional antiferromagnetic topological insulator, *Nature Mater.* **19**, 522 (2020).

[41] H. Deng, *et al.*, High-temperature quantum anomalous Hall regime in a $MnBi_2Te_4/Bi_2Te_3$ superlattice, *Nature Phys.* **17**, 36 (2021).

[42] D. Ovchinnikov, *et al.*, Intertwined Topological and Magnetic Orders in Atomically Thin Chern Insulator $MnBi_2Te_4$, *Nano Lett.* **21**, 2544 (2021).

[43] S. Yang, *et al.*, Odd-even layer-number effect and layer-dependent magnetic phase diagrams in $MnBi_2Te_4$, *Phys. Rev. X* **11**, 011003 (2021).

[44] A. Gao, *et al.*, Layer Hall effect in a 2D topological axion antiferromagnet, *Nature* **595**, 521 (2021).

[45] L. Tai, *et al.*, Distinguishing two-component anomalous Hall effect from topological Hall effect in magnetic topological insulator $MnBi_2Te_4$., *ACS Nano* **16**, 17336 (2022).

[46] S.-K. Bac, *et al.*, Topological response of the anomalous Hall effect in $MnBi_2Te_4$ due to magnetic canting, *npj Quantum Materials* **7**, 1 (2022).

[47] T. Akamatsu, *et al.*, A van der Waals interface that creates in-plane polarization and a spontaneous photovoltaic effect, *Science* **372**, 68 (2021).

[48] A. Iyama, T. Kimura, Magnetoelectric hysteresis loops in Cr_2O_3 at room temperature, *Phys. Rev. B* **87**, 180408 (2013).

[49] S. Jiang, J. Shan, K. F. Mak, Electric-field switching of two-dimensional van der Waals magnets, *Nature Mater.* **17**, 406 (2018).

[50] H. Zhang, *et al.*, Topological insulators in Bi_2Se_3, Bi_2Te_3 and Sb_2Te_3 with a single Dirac cone on the surface, *Nature phys.* **5**, 438 (2009).

[51] J. Kipp, *et al.*, The chiral Hall effect in canted ferromagnets and antiferromagnets, *Commun. Phys.* **4**, 99 (2021).

[52] All data in the main text and supplementary materials, as well as the codes for theoretical calculations of the quantum metric, are available from zenodo xxx.

Author contributions: SYX conceived the experiments and supervised the project. AG fabricated the devices, performed the measurements and analyzed data with help from YFL, DB, JXQ, HCL, CT, TD, ZS, SCH, DCB and QM. AG and SWC performed the microwave rectification experiments. CH, TQ and NN grew the bulk $MnBi_2Te_4$ single crystals. BG made the theoretical studies including first-principles calculations and effective modeling with the help from TVT, YO, SWL, BS, HL, AB, TRC, LF and PPO. TVT developed the effective model with help from BG under the guidance of PPO. KW and TT grew the bulk hBN single crystals. SYX, AG and QM wrote the manuscript with input from all authors.

Acknowledgement: We gratefully thank Amir Yacoby for his generous help for the microwave measurements. We also thank Marie Wesson and Nick Poniatowski for technical support during the microwave measurements. We thank Yang Gao and Junyeong Ahn, Philip Kim for helpful discussions. We also gratefully thank Linda Ye, Masataka Mogi, Yukako Fujishiro, and Takashi Kurumaji for extensive discussions on the scaling of AHE. Work in the SYX group was partly supported through the Center for the Advancement of Topological Semimetals (CATS), an Energy Frontier Research Center (EFRC) funded by the U.S. Department of Energy (DOE) Office of Science (fabrication and measurements), through the Ames National Laboratory under contract DE-AC0207CH11358. and partly through AFOSR grant FA9550-23-1-0040 (data analysis and manuscript writing). SYX acknowledges the Corning Fund for Faculty Development. QM acknowledges support from the CIFAR Azrieli Global Scholars program. SYX and DB were supported by the NSF Career DMR-2143177. CT and ZS acknowledge support from the Swiss National

Science Foundation under project P2EZP2_191801 and P500PT_206914, respectively. YFL, SYX, DCB, YO and LF were supported by the STC Center for Integrated Quantum Materials (CIQM), NSF Grant No. DMR-1231319. This work was performed in part at the Center for Nanoscale Systems (CNS) Harvard University, a member of the National Nanotechnology Coordinated Infrastructure Network (NNCI), which is supported by the National Science Foundation under NSF award no.1541959. Work at UCLA was supported by the DOE, office of Science, office of Basic Energy Sciences under Award Number DE-SC0021117. The work at Northeastern University was supported by the Air Force Office of Scientific Research under award number FA9550-20-1-0322, and it benefited from the computational resources of Northeastern University's Advanced Scientific Computation Center (ASCC) and the Discovery Cluster. The work in the QM group was partly supported through the CATS, an EFRC funded by the DOE Office of Science, through the Ames National Laboratory under contract DE-AC0207CH11358 (fabrication and measurements) and partly through NSF DMR-214342 (data analysis and manuscript writing). The work in the PPO group was supported from the CATS, an EFRC funded by the DOE Office of Science, through the Ames National Laboratory under contract DE-AC0207CH11358. TRC was supported by the Young Scholar Fellowship Program from the MOST in Taiwan, under a MOST grant for the Columbus Program, no. MOST110-2636-M-006-016, NCKU, Taiwan, and National Center for Theoretical Sciences, Taiwan. Work at NCKU was supported by the MOST, Taiwan, under grant no.MOST107-2627-E-006-001 and Higher Education Sprout Project, Ministry of Education to the Headquarters of University Advancement at NCKU. K.W. and T.T. acknowledge support from JSPS KAKENHI (Grant Numbers 19H05790, 20H00354 and 21H05233). MH and CRD were supported by the Air Force Office of Scientific Research under award No. FA9550-20-1-0319.

Competing financial interests: The authors declare no competing financial interests.

Data and materials availability: All data in the main text and supplementary materials, as well as the code for peak fitting, are available from Zenodo [52].

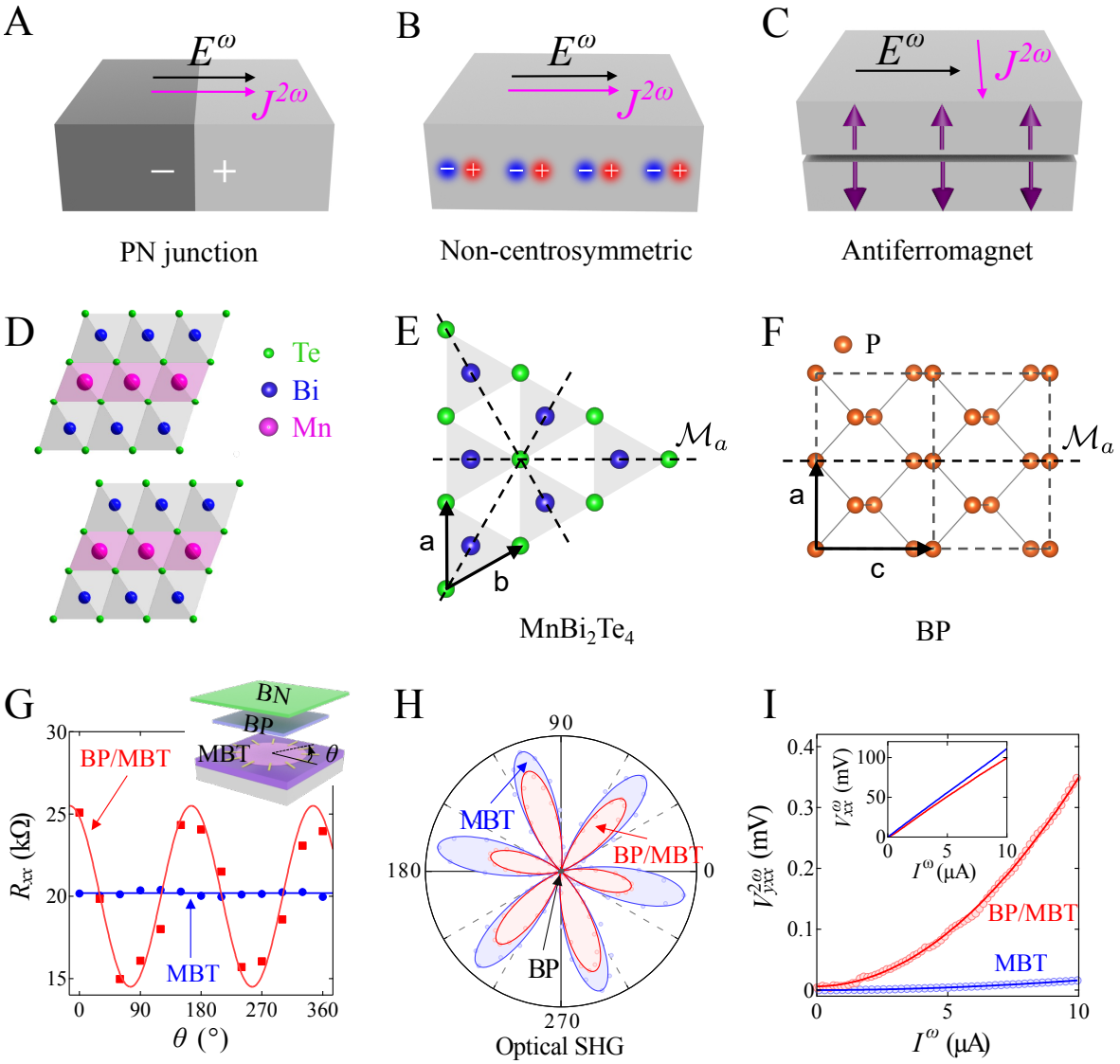

FIG. 1: **Spin-induced electrical nonlinearity in $\mathcal{PT}$-symmetric antiferromagnets and introduction to our sample.** (**A** and **B**) Nonlinear electrical transport in PN junctions and noncentrosymmetric conductors (charge-induced electrical nonlinearity). (**C**) Nonlinear electrical transport in $\mathcal{PT}$-symmetric AFMs (spin-induced electrical nonlinearity). (**D** to **F**) Lattice structures of the $MnBi_2Te_4$ and BP. (**G** and **H**) Angle-resolved resistance and optical second-harmonic generation (SHG) measurements of a 6SL $MnBi_2Te_4$ before and after interfaced with BP (Device-BM1). (**I**) The nonlinear Hall signal $V_{yxx}^{2\omega}$ of Device-BM1 before and after interfaced with BP at $B = 0$ T.

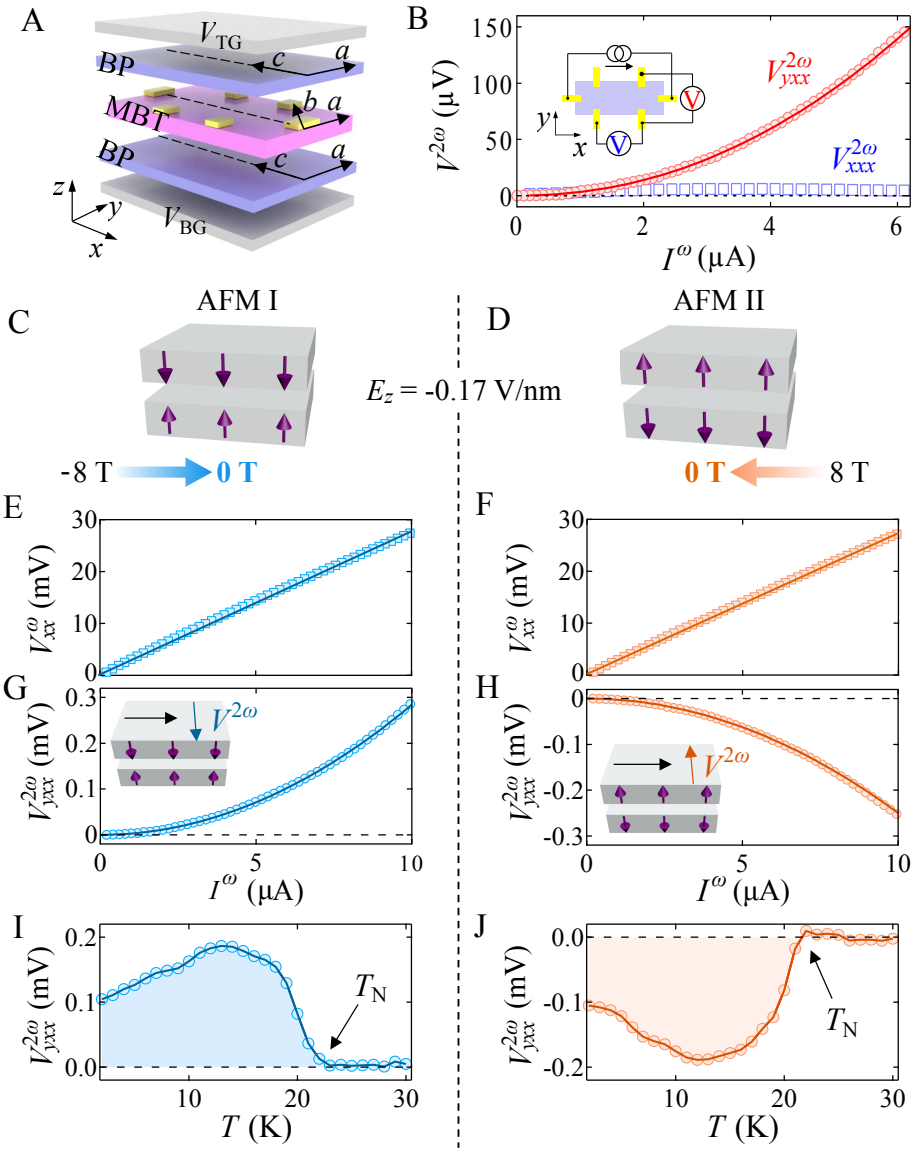

FIG. 2: **Observation of the antiferromagnetic nonlinear Hall effect.** (**A**) Schematic illustration of 2L BP/6SL $MnBi_2Te_4$/2L BP device (Device-BMB1). The crystalline a axes of the BPs and the $MnBi_2Te_4$ were all aligned (see fig. S16). (**B**) The longitudinal ($V^{2\omega}_{xxx}$) and Hall ($V^{2\omega}_{yxx}$) components of the nonlinear voltage. (**C** and **D**) We follow the procedures established by previous works [44]: under a fixed E_z (−0.17 V/nm), we sweep B_z from −8 T to 0 T or from +8 T to 0 T to prepare the two AFM states. (**E** and **F**) Linear longitudinal voltage as a function of incidence current for AFM I and AFM II. (**G** and **I**) Nonlinear Hall voltage as a function of incident current and temperature of AFM I. (**H** and **J**) The same as panels (G) and (I) but for AFM II.

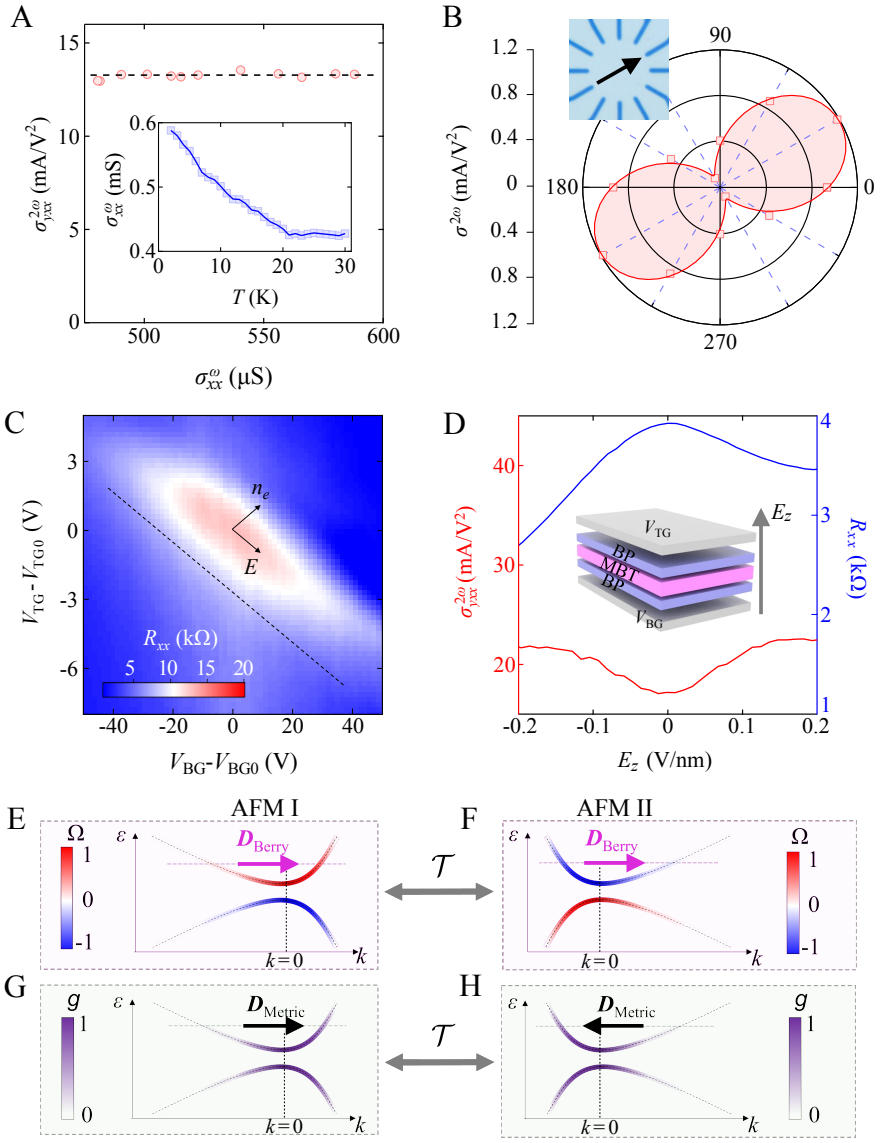

FIG. 3: **Systematic investigations of the nonlinear Hall effect.** (**A**) The scaling between the nonlinear Hall conductivity and the Drude conductivity $\sigma_{xx} = 1/R_{xx}$. The nonlinear Hall conductivity can be directly extracted from the data as $\sigma^{2\omega}_{yxx} = \frac{V^{2\omega}_{yxx}}{I^{\omega 2}_{x} R^{3}_{xx}} \frac{l^3}{w^2 d}$. (**B**) Angular dependence of the nonlinear Hall conductivity $\sigma^{2\omega}$ in Device-BM1. (**C**) Dual gated resistance map of the 2L BP/6SL $MnBi_2Te_4$/2L BP heterostructure (Device-BMB1). The vertical electric field E_z and charge density dependence can be independently tuned by combining the top and bottom gate voltages. (**D**) E_z dependence of the nonlinear Hall conductivity $\sigma^{2\omega}_{yxx}$ and linear longitudinal resistance R_{xx}. E_z follows the dashed line in (C). (**E** to **H**) Schematic illustration of the Berry curvature dipole (D_{Berry}) and quantum metric dipole (D_{Metric}) for the AFM I and AFM II of the BP/6SL $MnBi_2Te_4$/BP heterostructure . Although we aligned the crystalline axes of BP and $MnBi_2Te_4$ in our Device-BMB1 (Fig. 2A), realistically it is difficult to make alignment perfect. If the alignment is imperfect and $\mathcal{PT}$ symmetry is broken, a Berry curvature dipole is allowed.

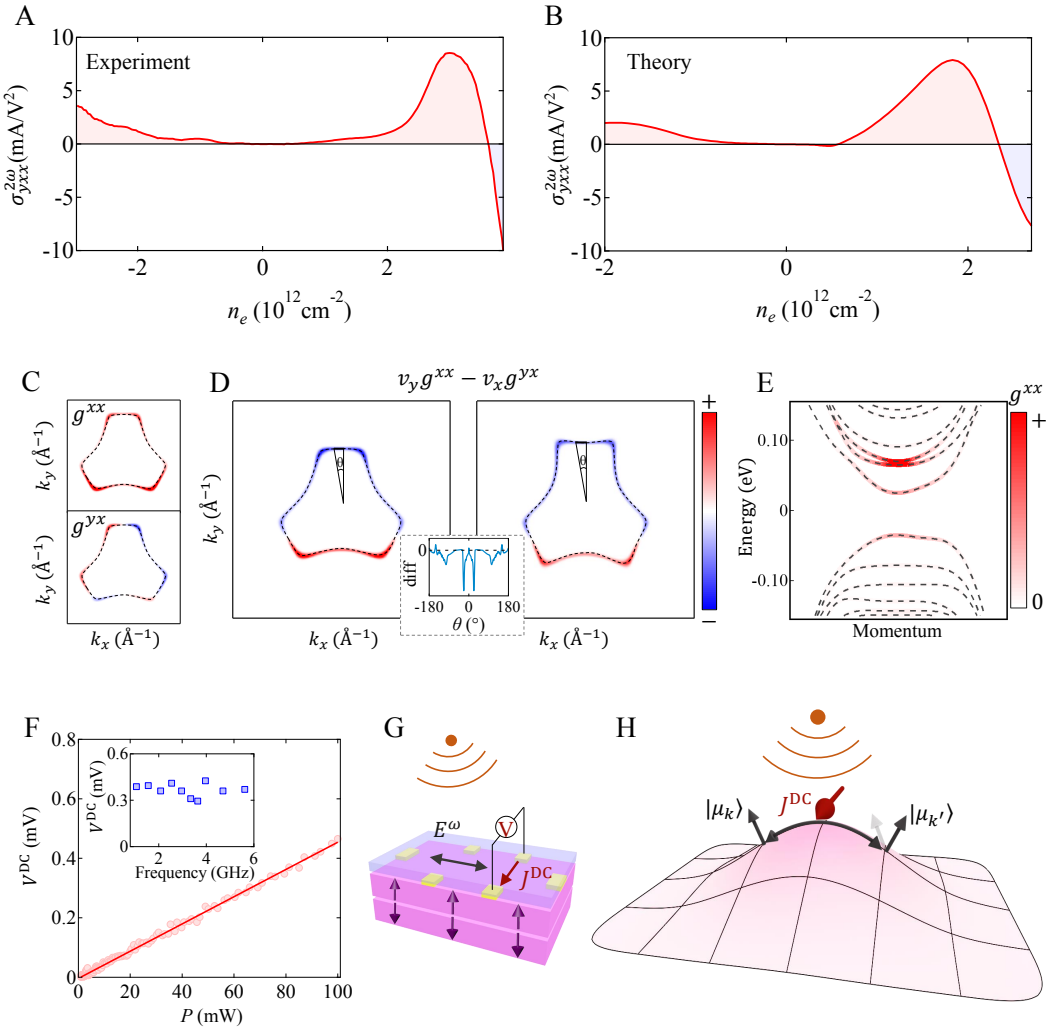

FIG. 4: **The quantum metric dipole as the microscopic geometrical origin.** (**A**) Experimentally measured nonlinear Hall conductivity $\sigma^{2\omega}_{yxx}$ as a function of charge density n. (**B**) Theoretically calculated $\sigma^{2\omega}_{yxx}$ as a function of n based on the BP/6SL $MnBi_2Te_4$/BP band structure (see text). (**C** to **E**) The electronic structure of the BP/6SL $MnBi_2Te_4$/BP heterostructure calculated with an effective model (see text). (**C**) Fermi surface at -50 meV (the lower part of the surface Dirac cone). The coupling between $MnBi_2Te_4$ and BP is turned off, so that contour respects C_{3z} symmetry. The quantum metric g_{xx} and g_{yx} plotted around the Fermi surface. (**D**) The nonlinear Hall conductivity $\sigma^{2\omega}_{yxx}$ is given by the integral of $(v_y g_{xx} - v_x g_{yx})$ around the Fermi surface. $D_{\text{Metric}} = \int_{\mathbf{k}} (v_y g_{xx} - v_x g_{yx}) \delta(\varepsilon - \varepsilon_{\text{F}}) = \int_{\text{FS}} (v_y g_{xx} - v_x g_{yx}) dl$ (dl is an infinitesimal length along the Fermi surface (FS)). With C_{3z} symmetry (left panel), the integral goes to zero. After turning on the coupling between $MnBi_2Te_4$ and BP (right panel), C_{3z} is broken, making the integral of $(v_y g_{xx} - v_x g_{yx})$ around the Fermi contour nonzero. To more clearly see how the integral changes to nonzero when C_{3z} is broken, we rewrite D_{Metric} as an integral of the polar angle θ, $D_{\text{Metric}} = \int_{-\pi}^{+\pi} (v_y g_{xx} - v_x g_{yx}) (\frac{dl}{d\theta}) d\theta$. The inset presents the change of $(v_y g_{xx} - v_x g_{yx}) (\frac{dl}{d\theta})$, which clearly shows that the integral becomes nonzero when C_{3z} is broken. See SM.III.14 for details.

FIG. 4: (**E**) Band structure of BP/6SL $MnBi_2Te_4$/BP heterostructure. Color represents the quantum metric g_{xx} of the bands. (**F**) Measured microwave rectification based on the intrinsic nonlinear Hall effect. Inset is the DC signal V^{DC} as a function of microwave frequency. (**G**) Schematic illustration of microwave rectification. (**H**) Schematic illustration of quantum metric induced nonlinear responses. The horizontal axes are k_x and k_y. The two black arrows represent the Bloch wavefunctions at two nearby k points. The two arrows point to different directions, illustrating a finite distance between two wavefunctions (i.e., a finite quantum metric). This quantum metric leads to a nonlinear Hall effect, which can turn an external AC electric field (e.g. the microwave in the figure) into DC signal (J_{DC}).